Available online at www.sciencedirect.com

SciVerse ScienceDirect

Ceramics International 38 (2012) 3519–3527

CERAMICS INTERNATIONAL

www.elsevier.com/locate/ceramint

SiC whisker reinforced multi-carbides composites prepared from B_4C and pyrolyzed rice husks via reactive infiltration

Hongyan Wu [a], Mingxia Gao [a,*], Dan Zhu [a], Shengcai Zhang [a], Yi Pan [a], Hongge Pan [a], Yongfeng Liu [a], Filipe J. Oliveira [b], Joaquim M. Vieira [b]

[a] State Key Laboratory of Silicon Materials & Department of Materials Science and Engineering, Zhejiang University, Hangzhou 310027, PR China
[b] Department of Ceramics and Glass Engineering/CICECO, University of Aveiro, Aveiro 3810-193, Portugal

Received 7 November 2011; received in revised form 3 December 2011; accepted 22 December 2011
Available online 2 January 2012

Abstract

SiC whisker reinfored carbide-based composites were fabricated by a reactive infiltration method by using Si as the infiltrate. Rice husks (RHs) were pyrolyzed to SiC whiskers, particles and amorphous carbon, and were then mixed with different contents of B_4C as well as Mo powders. The mixtures were molded to porous preforms for the infiltration. The SiC whiskers and particles in the preform remained in the composite. Molten Si reacted with the amorphous carbon, B_4C as well as Mo in the preform during the infiltration, forming newly SiC, $B_{12}(C,Si,B)_3$ as well as $MoSi_2$. The upper values of elastic modulus, hardness and fracture toughness of the composites are 297.8 GPa, 16.8 ± 0.8 GPa, and 3.8 ± 0.2 MPa $m^{1/2}$, respectively. The influence of the phase composition of the composites on the mechanical properties and the fracture mechanism are discussed.

Keywords: B. Composites; C. Mechanical Properties; D. Carbides; Reaction infiltration; Pyrolyzed rice husks, Microstructure

1. Introduction

Carbide ceramics have high mechanical wear resistance, hardness, thermal and chemical stability. SiC ceramics are most important materials for advanced engineering applications due to their excellent high-temperature strength, high hardness, good oxidation, corrosion, wear and thermal shock resistance [1,2]. A variety of applications of the SiC ceramics in the industry can be found, including wear parts, light-weight armor, cutting tools, high temperature structural parts, etc. Hot-pressing and pressureless sintering are two common ways to prepare the SiC ceramics. However, the former needs extra pressure and the latter needs extremely high temperature, which all lead to high material fabrication cost and costly equipments. An alternative economic approach to fabricate dense SiC-based ceramics is reactive infiltration [3–5], in which green preforms or partially sintered preforms of carbon are infiltrated by molten Si, forming composites after solidification. The molten Si reacts with the carbon, forming SiC. The residual Si remains in the ceramics.

B_4C is one of the hardest materials of the world. Its hardness reaches as high as 27–35 GPa. The application of the B_4C ceramics in industry is also extremely important [6,7]. The reactive infiltration method is also applicable to fabricate B_4C-based ceramics by infiltrating molten Si into B_4C-based preforms [8–10]. In the B_4C/Si infiltration system, Si reacted with B_4C, forming newly SiC and other boron-rich carbides [8,9].

In the recent years, multi-carbides ceramics based on B_4C and SiC are considered to be able to provide improved mechanical properties compared with the single carbide ceramics [9,11–15]. SiC and boron-rich carbides were formed in situ in the fabrication process [12–15]. It was reported that the in situ formed SiC in the $(SiC,TiB_2)/B_4C$ composites introduced new grain boundaries, leading to a higher grain boundary energy and a higher crack propagation resistance, thus improving the fracture toughness of the composite.

Introduction of whiskers or fibers is an effective strategy in improving the fracture tolerance and/or the strength of ceramics [16]. SiC whiskers (SiC_w) are promising material in strengthening and toughening composite ceramics and light metal alloys for

* Corresponding author. Tel.: +86 571 87952615; fax: +86 571 87952615.
E-mail address: gaomx@zju.edu.cn (M. Gao).

0272-8842/$36.00
doi:10.1016/j.ceramint.2011.12.065

structural use [17]. SiC_w can enhance crack bridging and deflection and in turn resulting in improved fracture toughness [18]. An economic route to prepare SiC_w is the pyrolysis of the rice husks (RHs), but high content of amorphous carbon also exists in the product. Previous studies were mostly focused on the fabrication technique of the SiC_w and the structure analysis of the pyrolyzed RHs [19–23]. The study of the utilization of the pyrolyzed RHs is hardly reported. Moreover, the separation of the SiC_w and the carbon is difficult. Therefore, the practical application of the SiC_w produced from pyrolyzed RHs has also not been realized. RHs were produced year by year all over the world, and they are mostly taken as agricultural wastes. The study of the RHs converted SiC whiskers and also the SiC particles as well as carbon in the application of ceramic materials should be a meaningful work.

In the present work, RHs were converted to SiC whiskers and particles as well as carbon, which were used as one of the starting materials to fabricate SiC whisker introduced carbides-based composites. The pyrolyzed RHs were mixed with B_4C as well as a little amount of Mo, and molded to porous preform, which was subsequently infiltrated by molten Si. Molten Si is supposed to react with the carbon and B_4C in the preform, forming newly carbides. The SiC whiskers and particles in the preform will be preserved in the composite. The addition of Mo is intended to form $MoSi_2$ by the reaction with Si, which is hopefully favorable to the overall properties of the composites, as $MoSi_2$ is a less brittle phase compared with Si and it has a high melting temperature of 2030 °C, favoring high temperature properties of the composite. The microstructure and mechanical properties including elastic modulus, fracture toughness and hardness of the composites have been studied. For comparison, parallel studies of the composite prepared from preform without Mo addition were also conducted. The results are hopefully to be able to provide some new experiment results for the use of RHs in the fabrication of ceramic materials.

2. Experimental

Raw RHs were pre-treated by washing, drying and sieving to eliminate the residual rice and clay particles firstly, and then were coked at 900 °C for 2 h in vacuum in a tube furnace. The intermediate coke was further pyrolyzed at 1550 °C for 6 h under Ar atmosphere in a graphite furnace. A heating rate of 10 °C/min and furnace cooling were used. The pyrolyzed RHs powder was mixed with purchased B_4C as well as metallic Mo by ball-milling with agate balls for 3 h at a rate of 650 rpm. Alcohol was used as milling medium. The composition of the mixtures is listed in Table 1. The particle size of B_4C ranges from 5 to 10 μm (Dalian Jinma Technology Co., Ltd., China. The residual free carbon is ca. 1.8 wt.%), and the particle size of Mo powder is ca. 3 μm. Fig. 1(a) is a scanning electron microscopy (SEM, S-4800, Hitachi) morphology of the as-purchased B_4C. The mixtures were dried and molded to porous preforms with dimension of 50 mm × 50 mm × 5 mm by being uniaxially cold pressed at 96 MPa in a stainless steel mold. The preforms were pre-sintered at 1550 °C for 2 h prior to the infiltration in order to release the organic ingredients and intend to increase the relative density of the preforms. The apparent density of the pre-sintered preforms was estimated according to their mass and volume. The volume of the preforms was measured by a conventional Vernier calliper. A balance with accuracy of 0.1 mg was used for weighing in the present study. The theoretical density of the performs was calculated by the equation of

Table 1
The composition and the relative density of the preforms.

Samples	The composition of green preforms (wt.%)			The relative density of the preforms (%)
	Pyrolyzed HRs	B_4C	Mo	
S1	20	70	10	50
S2	40	50	10	48
S3	60	30	10	46
S4	66.7	33.3	0	46

$$d_T = \frac{\sum M_i}{\sum M_i/d_i} \quad (1)$$

where M_i is the mass of the B_4C, free carbon, SiC and Mo in the preform. d_i is the theoretical density of B_4C, carbon, SiC and Mo, which is taken as 2.52, 1.85, 3.21 g/cm^3 and 6.28 g/cm^3, respectively. The relative density of the preforms is denoted as the percentage of the apparent density to its theoretical density. The recorded value of the relative density for each preform is the average of five pieces.

Infiltration was performed at 1480 °C × 30 min. The heating and cooling rates were 5 and 10 °C/min, respectively, for both the pre-sintering and infiltration. Sufficient Si fragments, the amount of which was estimated by pre-testing were put on the top of the preform. Both the pre-sintering and the infiltration were carried out in a graphite furnace under a vacuum of 10^{-2} Pa.

The phase structure of the pyrolyzed RHs and the composites was analyzed by X-ray diffraction (XRD, PANalytical, X'Pert PRO) using Cu Kα radiation (λ = 1.54056 Å) with a step interval of 0.02° and a count time of 1 s per step. The phase composition of the composites was further analyzed by XRD Rietveld refinement method. The morphology of the pyrolyzed RHs was observed by SEM. The microstructure of the composites was observed by both SEM and optical microscopy (OM, Leica, DMLM). Energy dispersive spectrometry (EDS, Horiba) under SEM was used in the estimation of the compositions of the pyrolyzed RHs and the phases in the composites. The content of free carbon of the pyrolyzed RHs was estimated roughly by a burning method based on the previous study [24], i.e., heating the pyrolyzed RHs at 700 °C for 3 h in air atmosphere and then measuring the weight loss, which was supposed to be caused by the oxidation of the free carbon. The microstructure of the composites was observed on their polished sections.

The infiltrated parts were cut into bars and further grounded with a diamond plated wheel of 0.5 μm as final for Vickers hardness and fracture toughness tests. Hardness of the

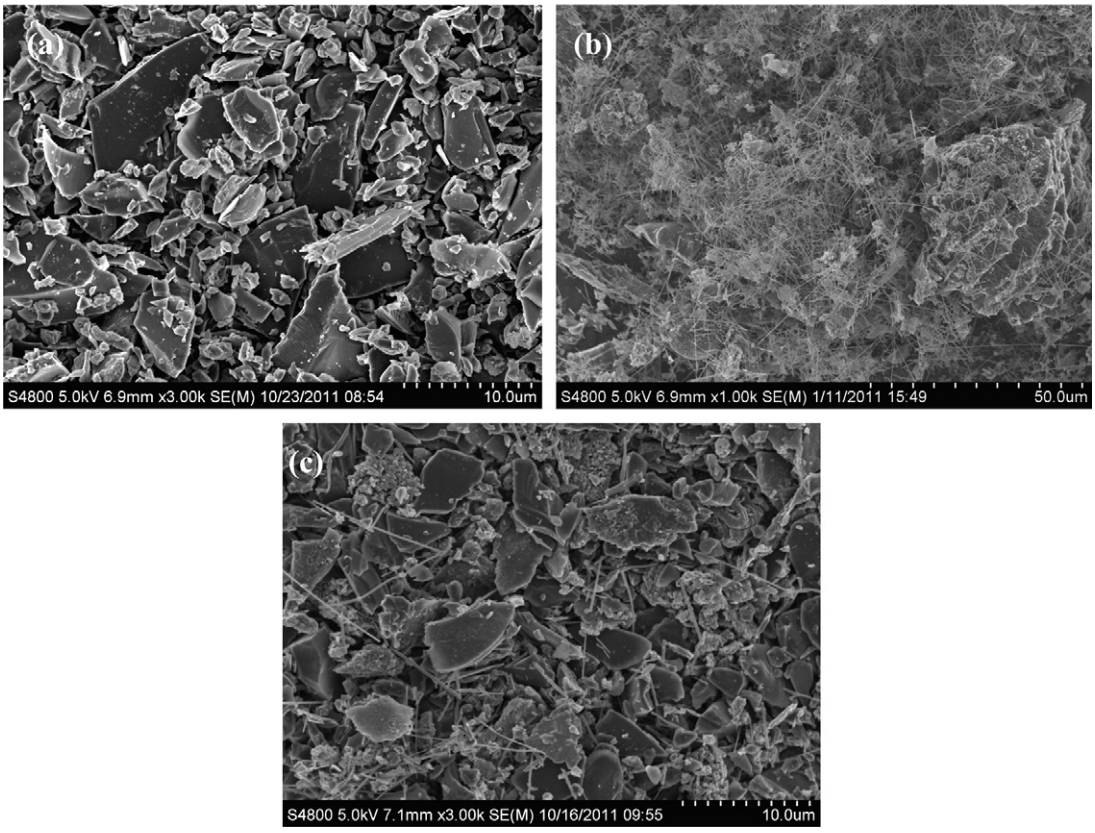

Fig. 1. SEM micrographs of the purchased B_4C (a), the as-pyrolyzed RHs (b), and the ball-milled mixture of 60 wt.% pyrolyzed RHs–30 wt.% B_4C–10 wt.%Mo (c).

composites was analyzed by a Vickers diamond pyramid indenter with a load of 9.8 N and a dwelling time of 10 s. The elastic modulus of the composites was measured by ultrasonic technique (Olympus, 5072PR). Indentation fracture toughness of the composites was evaluated by the following equations:

1. Niihara's model [25]:

$$K_{IC} = 0.035 H_v \frac{1}{\phi} a^{1/2} \left(\frac{c}{a} - 1\right)^{-1/2} \left(\frac{E\phi}{H_v}\right)^{2/5} \quad (2)$$

2. Evans's model [26]:

$$K_{IC} = H_v \sqrt{a} \left[\frac{E}{H_v}\right]^{0.4} 10^{f(x)} \quad (3)$$

$$f(x) = -1.59 - 0.34x - 2.02x^2 + 11.23x^3 - 24.97x^4 + 16.23x^5$$

$$x = \log_{10}\left(\frac{c}{a}\right)$$

where c is the half length between the tips of two faced indentation cracks of the Vickers indentation and, a, the half length of the diagonal of the indentation, E, the elastic modulus, H_v, the hardness, Φ, a constant of 2.7. Values of c and a in the present study were measured under OM. The applicability of Niihara's model is that the ratio of c to a (c/a) should be in the range of 1.25 to 3.5 [25], and the value of c/a should be in the range of 1.5 to 7.0 for Evans's model [26]. Values of Vickers hardness and fracture toughness reported for each composite are the averages of at least five tests. The microhardness of the phases of the composites was measured by a microhardness tester (MH-5, Shanghai, China) under a load of 100 g dwelling for 10 s, and at least 20 points were tested for each phase. Additionally, the fracture surface and the Vickers indentation cracks of the composites were also observed by SEM.

3. Results and discussion

3.1. Structure characterization of the pyrolyzed RHs and the composites

The typical SEM micrograph of the pyrolyzed RHs is displayed in Fig. 1(b). One can see clearly that two distinct morphologies, whiskers and particles, formed in the product. But the whiskers and particles are not homogenously distributed. The length of the whiskers is from several microns to several tens of microns, and the diameter of the whiskers is in the range of 100–300 nm. Fig. 1(c) is a SEM micrograph of the mixture of the pyrolyzed RHs, B_4C as well as Mo after the ball milling, which is from sample S3 (Table 1). It is seen that the distribution of the SiC whiskers is much homogenous after the ball-milling. XRD patterns of the pyrolyzed RHs as well as the purchased B_4C are displayed in Fig. 2. β-SiC is the main crystal phase of the pyrolyzed RHs product. The peak located at around 26° in the pattern of the pyrolyzed RHs is from carbon. The wide peak width indicates its poor crystallinity. Carbon peak is

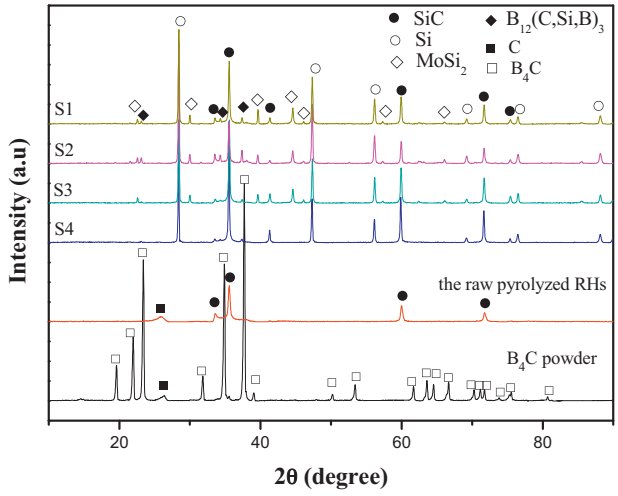

Fig. 2. XRD patterns of the composites prepared from preforms with different proportions of the pyrolyzed RHs and B_4C (samples of S1, S2, S3 and S4 in Table 1), the pyrolyzed RHs and the B_4C powders.

also found in the raw B_4C powder, which confirms the existence of free carbon in the as-supplied B_4C powder. EDS analysis under SEM shows that the main constituents of the pyrolyzed RHs are C (ca. 79 wt.%) and Si (ca. 17 wt.%). Besides, minor amount of O (ca. 3 wt.%) and negligible amount of Ca and other impure elements (less than 1 wt.% for total amount) were also detected. The oxygen is supposed from SiO_2 mainly. However, due to that the resolution of EDS for the light elements such as C and O is low, the composition of the pyrolyzed RHs reported is semi-quantitative. The content of free carbon of the pyrolyzed RHs tested by the burning method was ca. 65 wt.%, which should be the maximum for the content of free carbon, as partial SiC and the remained minor organic substances such as SiO_2 could be decomposed in the burning process, causing extra weight loss.

The relative densities of the pre-sintered preforms with different proportions of the pyrolyzed RHs and B_4C are also listed in Table 1. It is seen that the relative density of the preform decreases with the increasing amount of the pyrolyzed RHs. Moreover, the preform with comparable weight ratio of pyrolyzed RHs to B_4C does not show evident difference in the relative density, as seen from samples S3 with S4. In addition, the pre-sintering of 1550 °C × 2 h almost does not cause any change in the relatively density of the prefroms.

The quality of the infiltrated samples was firstly judged by macroscopic observation. The composite surfaces have smooth and dense appearance, except for sample S3, in which surface flaws was found. The densities of the composites are listed in Table 2. Similar as the relative density of the preform, the density of the composites also increases with the amount of the pyrolyzed RHs in the preform. The density of the composite without Mo addition is slightly lower than that of the one with Mo addition from preforms with similar weight ratio of the pyrolyzed RHs to B_4C.

The XRD patterns of the composites are also displayed in Fig. 2. As seen from Fig. 2, SiC, $B_{12}(C,Si,B)_3$ and Si are the main phases in the composites. For the samples with Mo addition in the preform, $MoSi_2$ was formed via the reaction of Mo and Si. The original added B_4C almost could not be detected in the composites. The formation of the new ternary boron-rich carbide of $B_{12}(C,Si,B)_3$ by the reaction of B_4C and molten Si during the infiltration of molten Si into porous B_4C preform was also reported in previous literature [8,10]. Diffraction signal of carbon is hardly found in the composites, indicating that the free carbon either in the pyrolyzed HRs or in the raw B_4C reacted mostly with Si, forming newly carbides.

Table 2
The phase contents and the density of the composites prepared from preforms with different proportions of pyrolyzed RHs and B_4C.

Samples	Phase contents (wt.%)				Density (g/cm^3)	
	SiC	$B_{12}(C,Si,B)_3$	Si	$MoSi_2$	Measured	Calculated
S1	29.6	40.5	26.2	3.7	2.68	2.69
S2	46.7	25.5	24.3	3.3	2.76	2.80
S3	60.9	12.6	23.4	3.5	2.89	2.90
S4	45.8	32.6	21.7	–	2.69	2.73

Goodness of fitting: the values of Sig and R_w (%) were 3 and 9, respectively.

The phase contents of the composites obtained from the XRD Rietveld refinement are also listed in Table 2. The theoretic density of the composites calculated from the phase contents is also listed in Table 2, where the theoretic density of $B_{12}(C,Si,B)_3$ and $MoSi_2$ is taken as 2.52 (from its JCPDS cards, No. 19-0178) and 6.28 g/cm^3, respectively. From Table 2, it is seen that the composites are highly dense. Further seen from Table 2, the content of SiC increases and accordingly that of $B_{12}(C,Si,B)_3$ decreases with the increasing proportion of the pyrolyzed RHs in the preform, which is related to a higher original contents of SiC (whisker and particles) and free carbon. The original SiC in the preform is maintained in the composite and the free carbon further reacted with Si forming newly SiC, causing the higher content of SiC in the composite.

To convert the weight percentage of the residual Si listed in Table 2 into volume percentage, a close value of ca. 29–30 vol.% is obtained for the composites with Mo addition despite the different proportions of the pyrolyzed RHs and B_4C in the preforms, and a slight lower value of 26 vol.% is obtained for the composite without Mo addition. The volume percentage of the residual Si in the composites is much lower than the porosity of the preforms. This indicates that large volume expansion occurred during the formation of the newly formed carbides, resulting in the reduction of the volume of the residual Si in the composite compared with the original free space of the preform. The slightly lower content of residual Si in the composite prepared from preform without Mo addition (sample S4) should be due to the slightly higher content of free carbon in the preform, which caused a slightly higher content of the carbides. The formation of surface flaws in sample S3 should also be due to the high content of free carbon as well as the existence of Mo in the preform which caused a high content of SiC and the formation of $MoSi_2$, both of which led to large volume expansion and severer strain after solidification.

Table 2 further shows that the apparent density of the composites (S1–S3) increases slightly with the ratio of the

pyrolyzed RHs to B_4C in the preforms, which is almost linearly correlated with the weight ratio of SiC to $B_{12}(C,Si,B)_3$ in the composites. The result is in accordance with the higher density of SiC compared with that of $B_{12}(C,Si,B)_3$. Additionally, the composite without Mo addition (sample S4) shows the lowest density among all of the composites. One of the possible reasons is that sample S4 lacks of $MoSi_2$, which has the largest density among all of the phases in the composites.

Fig. 3(a)–(d) displays the SEM micrographs of the composites prepared from preforms with different proportions of the pyrolyzed RHs and B_4C with and without Mo addition. SEM observations showed that the composites are almost dense inside, even for sample S3, which has surface flaws. Driven by the capillary pressure, Si infiltrated through and filled up almost all of the free space of the preform. Three visible contrasts can be found in Fig. 3(a)–(c), dark gray particles, light gray matrix and an offwhite phase, whereas no offwhite phase was observed in Fig. 3(d). Combining the results of XRD analysis mentioned above, it is identified that the dark gray particles are $B_{12}(C,Si,B)_3$; the light gray matrix involves both the Si phase and the SiC particles. SiC and Si have close contrast and they can only be vaguely distinguished under SEM. But compared with Si, SiC shows slightly lighter contrast. The offwhite phase in Fig. 3(a)–(c) is $MoSi_2$. The distribution of $MoSi_2$ is inhomogenous. Moreover, particles of slightly darker contrast were seen in some $B_{12}(C,Si,B)_3$ particles, but it was not so often. Fig. 4(a) displays a large magnification SEM image for showing the darker contrast inside the $B_{12}(C,Si,B)_3$ particle, which is from sample S2. Fig. 4(b) and (c) shows the result of the EDS analysis of the dark gray phase of $B_{12}(C,Si,B)_3$ and the slightly darker contrast inside, respectively. The corresponding composition of the two phases is also listed in Fig. 4(b) and (c). Due to the limited resolution of EDS for the light elements of C and B, the composition of the two phases is only semi-quantitative, however, Fig. 4(b) and (c) and their data are still helpful on identifying the phase with the darker contrast. Comparing Fig. 4(b) and (c), it is seen that the relative intensity of B and C is lower in Fig. 4(b) than that in Fig. 4(c). Moreover, only a minor fraction of Si was detected from the spectrum of Fig. 4(c), while the Si content is much higher as seen from Fig. 4(b). In addition, both phases are B rich, therefore, it is suggested that the darker phase is possibly B_4C. Due to the extremely low amount, B_4C was not detected by XRD. The dark gray phase is confirmed to be $B_{12}(C,Si,B)_3$. That partial B_4C remained in the B_4C/Si infiltration system was also reported in previous literature [8]. The mechanism of the formation of $B_{12}(C,Si,B)_3$ in the B_4C/Si infiltration system was considered to be a dissolution–precipitation process [8]. When the dissolution–precipitation process was not fully achieved, a core-rim structure with B_4C as core and $B_{12}(C,Si,B)_3$ as rim formed [8,9]. In the present study, B_4C transformed mostly to $B_{12}(C,Si,B)_3$ and only tiny amount remained, which may be due to the higher infiltration temperature and the longer isothermal dwelling time (1480 °C × 30 min) than those used in the literature (1450 °C × 15–20 min) [8,9], in which much amount of B_4C maintained. Almost complete transformation of B_4C to $B_{12}(C,Si,B)_3$ was also reported when infiltration parameters of 1480 °C × 15 min were used [8]. Moreover, small light gray particles inside some $B_{12}(C,Si,B)_3$ particles could also be found, as shown in Fig. 4(a). These light gray particles are SiC.

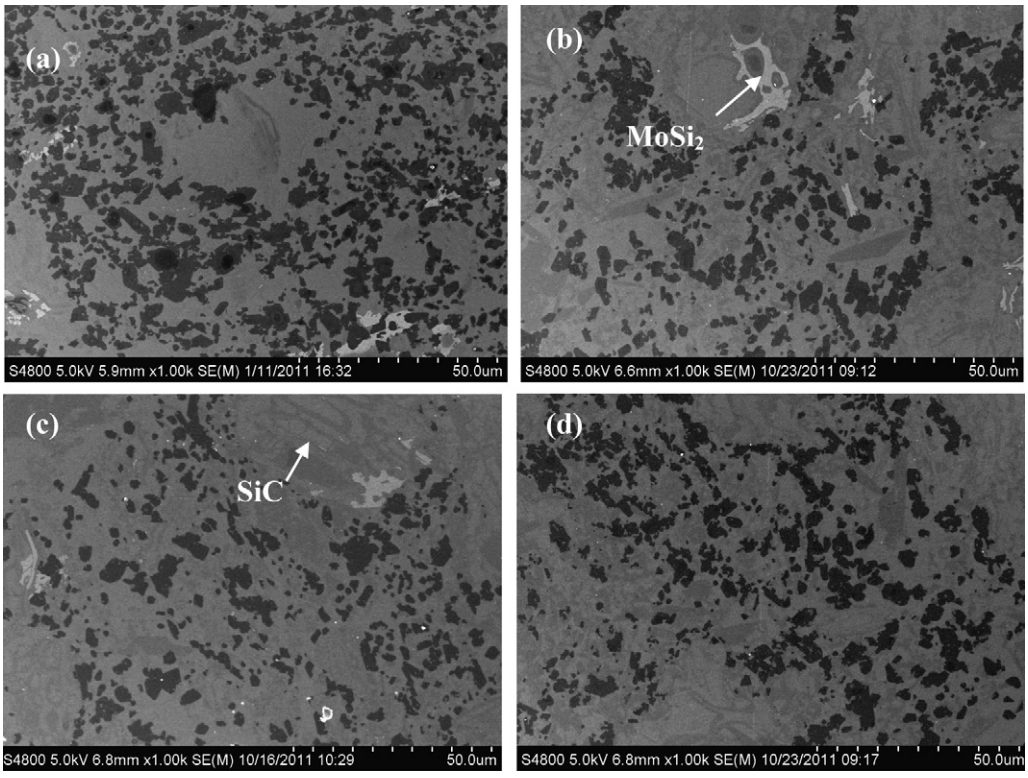

Fig. 3. SEM micrographs of the composites prepared from preforms with different compositions: (a) S1, (b) S2, (c) S3, and (d) S4.

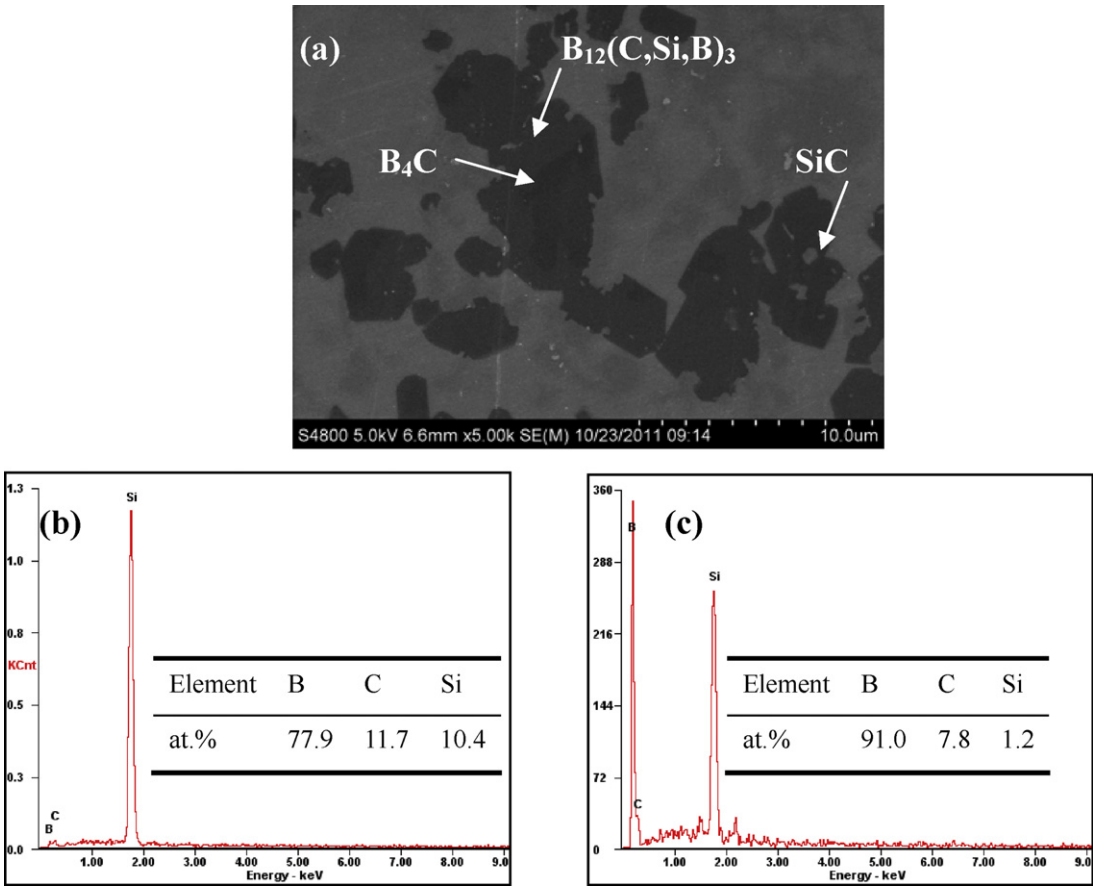

Fig. 4. A SEM image (from sample S2), which shows the darker contrast and the light gray particles inside the $B_{12}(C,Si,B)_3$ particles (a); EDS spectra for the compositions of the $B_{12}(C,Si,B)_3$ phase (b) and the darker phase inside the $B_{12}(C,Si,B)_3$ particles (c).

The formation of SiC inside the $B_{12}(C,Si,B)_3$ particles indicates the reaction of the free carbon inside the B_4C particles and/or the combined carbon from B_4C with molten Si.

Though SiC is difficult to be distinguished from Si by SEM, different contrast between SiC and Si was found by OM. Fig. 5 is a representative OM image of the composites, which is from sample S3. Different from the SEM images, SiC and $B_{12}(C,Si,B)_3$ turn to be difficult to be distinguished in the OM image, but basically, the $B_{12}(C,Si,B)_3$ phase displays slightly darker contrast compared with the SiC phase. Si shows slightly lighter contrast compared with both SiC and $B_{12}(C,Si,B)_3$. The write phase in Fig. 5 is $MoSi_2$. Further seen from Fig. 5, besides the graininess morphology, biomorphic morphology is observed often for the SiC phase. The biomorphic structure of the pyrolyzed carbon originally from RHs maintained to the SiC phase in the composites. Some of the SiC particles are of very small size, which is attributed to the original small carbon particles in the pyrolyzed RHs. The small SiC particles should favor the toughness of the composites. Unreacted carbon was occasionally found in the composite, as shown in Fig. 5. SiC whiskers cannot be distinguished at the polished cross-section of the composites either by SEM or by OM. However, from the strong etched fracture surface of the composite in which considerable Si was removed by the dissolution of NaOH, bare SiC whiskers are observed, as shown in Fig. 6, which is from sample S4. SiC whiskers derived from the preform are preserved in the composites.

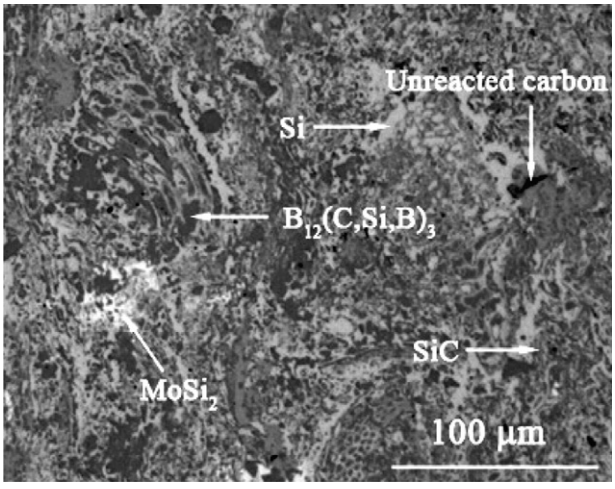

Fig. 5. A representative OM image of the composites, which is from sample S3.

3.2. Mechanical properties of the composites

The Vickers hardness, elastic modulus and indentation fracture toughness of the composites are listed in Table 3. The

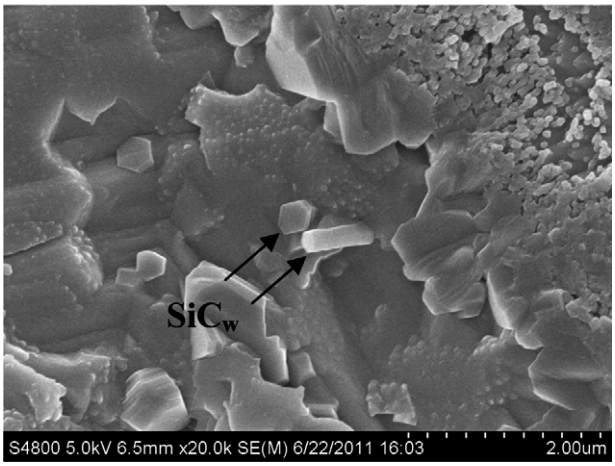

Fig. 6. A SEM micrograph of the fracture surface of the composite (sample S4) etched in 3 M/L NaOH for 18 h at room temperature, showing the SiC whiskers.

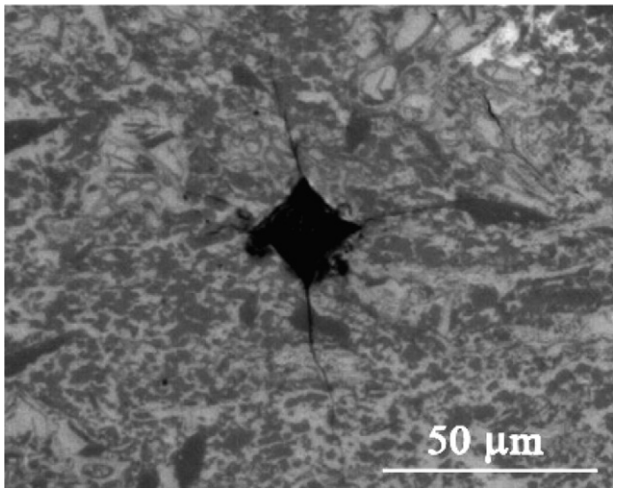

Fig. 7. A representative OM image of the Vickers indentation of the composites, which is from sample S2.

values of *c*/*a* of the Vickers indentation of the present composites are in the range of 2.13–3.07, which fit the requirement of Niihara's and Evens's models. Fig. 7 is a representative OM image of the diamond pyramid indentation of the composites, which is from sample S2. Table 3 shows that the Vickers hardness and the elastic modulus of the composites increase slightly with the content of the pyrolyzed RHs in the preforms (with Mo addition), which is corrected with the increase of the SiC content and the decrease of the $B_{12}(C,Si,B)_3$ content in the composites. While the fracture toughness shows an inverse variation tendency, but the difference is extremely small and almost can be ignored. The microhardness of SiC and $B_{12}(C,Si,B)_3$ particles is $23 \pm 2\ H_v$ and $27 \pm 2\ H_v$, respectively, and that of Si is 13 ± 1 H_v, as measured in the present study. As seen from Tables 2 and 3, the composite with lower content of the harder phase of $B_{12}(C,Si,B)_3$ does not correspond to a lower hardness and it even shows a slightly higher hardness. One of the relevant reasons is that the composite with lower content of $B_{12}(C,Si,B)_3$ has a higher content of the SiC whiskers due to the higher content of the pyrolyzed RHs in the preform, and the large amount of SiC whiskers acted as strong framework, increasing the hardness. Another possible factor that caused somewhat the higher hardness of the composite with lower content of $B_{12}(C,Si,B)_3$ is the slightly lower content of Si, which has low hardness. The hardness of the composite is compromised by the contribution from the different phases in the composites.

Table 3
Mechanical properties of the composites prepared from preforms with different contents of pyrolyzed RHs and B_4C.

Samples	Vickers hardness (GPa)	Elastic modulus (GPa)	Fracture toughness (MPa $m^{1/2}$)	
			Niihara	Evans
S1	15.4 ± 0.9	294.1	3.7 ± 0.3	3.9 ± 0.2
S2	16.2 ± 0.8	295.3	3.6 ± 0.5	3.8 ± 0.4
S3	16.8 ± 0.8	297.8	3.5 ± 0.3	3.8 ± 0.3
S4	16.4 ± 0.5	281.6	3.4 ± 0.4	3.7 ± 0.5

For the composite without Mo addition, the Vickers hardness, elastic modulus and fracture toughness are all slightly lower than those of the composite with Mo addition from the preform with similar proportion of the pyrolyzed RHs and B_4C, as seen from the values of the samples S3 and S4 listed in Table 3. Though the distribution of $MoSi_2$ is inhomogeneous in the composites, the addition of metal Mo in the preform favors the mechanical properties tested presently. Besides, $MoSi_2$ has high melting point and has very good oxidation resistance at high temperatures. The introduction of $MoSi_2$ into the composite is expected to be favorable to the overall properties of the composites.

Fig. 8 shows a representative SEM micrograph of the Vickers indentation crack of the composites under the load of 9.8 N, which is from sample S2. It reveals that both transgranular fracture of the $B_{12}(C,Si,B)_3$ phase and the debonding of the interface of $B_{12}(C,Si,B)_3$ and Si occur in the failure mode of the composite. As SiC could not be distinguished from Si, the failure mode of SiC could not be known from the SEM observation of the indentation cracks. But

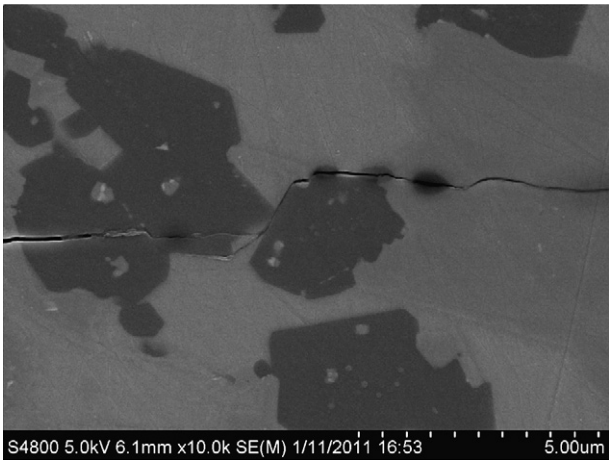

Fig. 8. A representative SEM micrograph of the Vickers indentation crack of the composites, which is from sample S2.

deflection of the cracks in the Si and SiC area were frequently observed, as shown also in Fig. 8. The deflection of the crack could be caused by the transgranular fracture of the SiC and Si phases, and could also be caused by the de-bonding of the interface of SiC and Si. The action of the SiC_w could not be educed from the indentation crack at the polished surface. However, from the fracture surface of the composites, Fig. 9(a)–(d), which is from sample S3, much information of the fracture characteristics is obtained. Fig. 9(a) is an overall image of the fracture surface. It is seen that two kinds of fracture features existed generally. One has large factured surfaces and the other has very small fractures surfaces. The area with the large fractured surfaces is suggested as being from the $B_{12}(C,Si,B)_3$ particles as well as the Si phase of large size. The size of the fracture area is consistent with that of the $B_{12}(C,Si,B)_3$ particles as displayed in Figs. 3–5. Moreover, transgranular cleavage is the main fracture mode of such area, as marked by "A" in Fig. 9(a). In addition, de-bonding of the carbide phase ($B_{12}(C,Si,B)_3$ probably) and the Si phase is also found in such area, as marked by "B", though it is not so frequently found. Fig. 9(b) is the amplification of the "B" area in Fig. 9(a), showing better the interfacial de-bonding of the carbide and Si phases. The results from Fig. 9(a) and (b) are consistent with those obtained from in Fig. 8. Fig. 9(c) is a large magnification image for showing the details of the fracture area with small fractured faces. This area is the reacted area of the pyrolyzed RHs with Si. Fine SiC particles, whiskers and biomorphic structures are involved in such area. Cavities of the pullout of the SiC whiskers (marked by "C"), the extrusion of the SiC whiskers (marked by "D") and the interfacial de-bonding of the mall SiC particles and Si (marked by "E") are seen. Moreover, most of the pullout of the SiC whiskers occurred at the tip of the whisker, indicating that the SiC whiskers were strong enough for transferring the load from the matrix to themselves. On the other hand, some of the pullout of the SiC_w display somewhat deep traces, indicating that the bonding strength of the SiC_w and the Si phase was still somewhat weaker with respect to the strength of the SiC_w. Si always displays a transgranular cleavage fracture mode. The small SiC particles also show weaker interfacial bonding strength with Si. As reported by Yang et al. [16], interfacial bonding between the reinforcement of SiC fiber/nanowire and the matrix should be neither too strong nor too weak. Some degree of fiber/nanowire pullout allows energy to be released in breaking the reinforcement–matrix bonding, which may result in an increased strength and toughness. The existence of interfacial de-bonding of the carbides and Si, including the SiC particles, especially for the small ones, and some of the $B_{12}(C,Si,B)_3$, suggested the somewhat weak interfacial strength, which should also favor the fracture toughness by providing energy absorbing fracture paths [27,28]. Mixed fracture modes of transgranular cleavage and de-bonding of the interfaces of the SiC whiskers, carbide particles and Si coexisted in the composites.

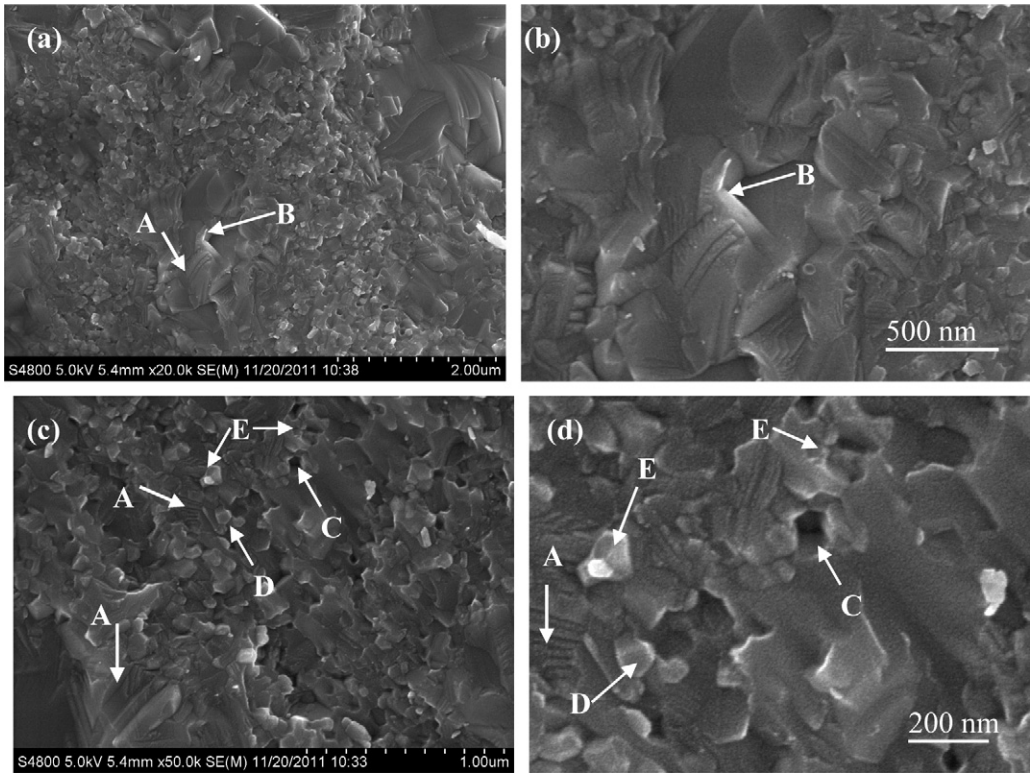

Fig. 9. Typical SEM micrographs of the fracture surfaces of the composites, which are from sample S3: (a) an overall image of the fracture surface; (b) the amplification of the marked area of (a); (c) a large magnification image for showing the details of the fracture features; (d) the amplification of the marked area of (c). (A: transgranular cleavage; B: Interfacial de-bonding of the carbide ($B_{12}(C,Si,B)_3$ probably) and Si; C: cavity of the pullout of SiC_w; D: extrusion of the SiC_w; E: interfacial de-bonding of the small SiC and Si).

4. Conclusions

Multi-carbides-based composites were fabricated by infiltrating molten Si into porous preforms prepared from mixtures of pyrolyzed RHs, which contained SiC whiskers, particles and amorphous carbon, and B_4C as well as Mo powders. The SiC whiskers and particles in the preform remained in the composites after infiltration. Molten Si reacted with the amorphous carbon and B_4C as well as Mo, forming newly SiC and $B_{12}(C,Si,B)_3$ as well as $MoSi_2$.

The content of SiC increases and that of $B_{12}(Si,C,B)_3$ decreases with the increasing proportion of the pyrolyzed RHs in the preform. Upper values of 16.8 ± 0.8 GPa, 297.8 GPa and 3.9 ± 0.2 MPa $m^{1/2}$ were obtained, respectively, for the Vickers hardness, elastic modulus and fracture toughness of the composites. The difference of the properties of the composites prepared from preforms with different compositions is small. Sufficient amount of SiC whiskers acted as strong framework, favoring the hardness of the composites. Mo addition favors the mechanical properties tested. Transgranular cleavage is the main fracture mode of the composites. But de-bonding of the interface of the carbides and Si, especially for the small SiC particles, coexisted in the fracture mode of the composites. Cavities of the pullout of SiC whiskers and the extrusion of the SiC whiskers also existed at the fracture surface of the composites.

Acknowledgment

The work was supported by The Science and Technology Program of Zhejiang Province, China (No. 2008C24002).

References

[1] Y.F. Hua, L.T. Zhang, L.F. Cheng, Z.X. Li, J.H. Du, Microstructure and mechanical properties of SiC_p/SiC and SiC_w/SiC composites by CVI, J. Mater. Sci. 45 (2010) 392–398.
[2] G. Amirthan, A. Udayakumar, V.V. Bhanu Prasad, M. Balasubramanian, Synthesis and characterization of Si/SiC ceramics prepared using cotton fabric, Ceram. Int. 35 (2009) 967–973.
[3] Y.M. Chiang, R.P. Messner, C.D. Terwilliger, D.R. Behrendt, Reaction-formed silicon carbide, Mater. Sci. Eng. A144 (1991) 63–74.
[4] A. Maity, D. Kalita, T.K. Kayal, T. Goswami, O. Chakrabarti, H.S. Maiti, P.G. Rao, Synthesis of SiC ceramics from processed cellulosic bio-precursor, Ceram. Int. 36 (2010) 323–331.
[5] J.N. Ness, T.F. Page, Microstructural evolution in reaction-bonded silicon carbide, J. Mater. Sci. 21 (1986) 1377–1397.
[6] W.K. Zhang, L.Z. Gao, J. Li, B.J. Yang, Y.S. Yin, TiAl/B_4C marine material—fabrication, mechanical and corrosion properties, Ceram. Int. 37 (2011) 783–789.
[7] C.X. Liu, J.L. Sun, Erosion behaviour of B_4C-based ceramic composites, Ceram. Int. 36 (2010) 1297–1302.
[8] S. Hayun, A. Weizmann, M.P. Dariel, N. Frage, Microstructural evolution during the infiltration of boron carbide with molten silicon, J. Eur. Ceram. Soc. 30 (2010) 1007–1014.
[9] S. Hayun, N. Frage, M.P. Dariel, The morphology of ceramic phases in B_xC–SiC–Si infiltrated composites, J. Solid State Chem. 179 (2006) 2875–2879.
[10] I. Mizrahi, A. Raviv, H. Dilman, M. Aizenshtein, M.P. Dariel, N. Frage, The effect of Fe addition on processing and mechanical properties of reaction infiltrated boron carbide-based composites, J. Mater. Sci. 42 (2007) 6923–6928.
[11] M. Patel, J. Subrahmanyam, V.V. Bhanu Prasad, R. Goyal, Processing and characterization of B_4C–SiC–Si–TiB_2 composites, Mater. Sci. Eng. A 527 (2010) 4109–4112.
[12] D. Mallick, T.K. Kayal, J. Ghosh, O.P. Chakrabarti, S. Biswas, H.S. Maiti, Development of multi-phase B–Si–C ceramic composite by reaction sintering, Ceram. Int. 35 (2009) 1667–1669.
[13] G. Magnani, G. Beltrami, G.L. Minoccari, L. Pilotti, Pressureless sintering and properties of αSiC–B_4C composite, J. Eur. Ceram. Soc. 21 (2001) 633–638.
[14] A. Li, Y.H. Zhen, Q. Yin, L.P. Ma, Y.S. Yin, Microstructure of (SiC, TiB_2)/B_4C composites by reaction hot pressing, Ceram. Int. 32 (2006) 849–856.
[15] G. Górny, M. Rgczk, L. Stobiersk, L. Wojnarb, R. Pampuch, Microstructure–property relationship in B_4C–βSiC materials, Solid State Ionics 101–103 (1997) 953–958.
[16] W. Yang, H. Araki, C.C. Tang, S. Thaveethavorn, A. Kohyama, H. Suzuki, T. Noda, Single-crystal SiC nanowires with a thin carbon coating for stronger and tougher ceramic composites, Adv. Mater. 17 (2005) 1519–1523.
[17] W. Yang, H. Araki, A. Kohyama, S. Thaveethavorn, H. Suzuki, T. Noda, Fabrication in situ SiC nanowires/SiC matrix composite by chemical vapour infiltration process, Mater. Lett. 58 (2004) 3145–3148.
[18] S.Y. Du, X.H. Zhang, P. Hu, W.B. Han, Effect of sintering temperature and holding time on the microstructure and mechanical properties of ZrB_2–SiC_w composites, Mater. Chem. Phys. 116 (2009) 76–80.
[19] K. Janghorban, H.R. Tazesh, Effect of catalyst and process parameters on the production of silicon carbide from rice hulls, Ceram. Int. 25 (1999) 7–12.
[20] R.V. Krishnarao, Y.R. Mahajan, Effect of acid treatment on the formation of SiC whiskers from raw rice husks, J. Eur. Ceram. Soc. 15 (1995) 1229–1234.
[21] L.Y. Sun, K.C. Gong, Silicon-based materials from rice husks and their applications, Ind. Eng. Chem. Res. 40 (2001) 5861–5877.
[22] V. Martínez, M.F. Valenica, J. Cruz, J.M. Mejía, F. Chejne, Production of β-SiC by pyrolysis of rice husk in gas furnaces, Ceram. Int. 32 (2006) 891–897.
[23] M. Andreoli, G.T. Luca, E.S. Miyamaru Seo, Characteristics of rice husks for chlorination reaction, Mater. Lett. 44 (2000) 294–298.
[24] J.G. Lee, I.B. Cutler, Formation of silicon carbide from rice hulls, Am. Ceram. Soc. Bull. 54 (2) (1975) 195–198.
[25] K. Niihara, R. Morena, D.P.H. Hasselman, Evaluation of K_{Ic} of brittle solids by the indentation method with low crack to indent ratios, J. Mater. Sci. Lett. 1 (1982) 13–16.
[26] A.G. Evans, in: S.W. Freiman (Ed.), Fracture Mechanic Applied to Brittle Materials, American society for Testing and Materials, Philadelphia, 1979 , pp. 112–135 (ASTM STP 678, part 2).
[27] C.M. Ward-Close, R. Minor, P.J. Doorbar, Intermetallic-matrix—a review, Intermetallics 4 (1996) 217–229.
[28] W.H. Tuan, W.B. Chou, H.C. You, S.T. Chang, The effects of microstructure on the mechanical properties of $A1_2O_3$–NiAl composites, Mater. Chem. Phys. 56 (1998) 157–162.